

Fat Quantification in Dual-Layer Detector Spectral Computed Tomography

Experimental Development and First In-Patient Validation

Isabel Molwitz, MD,* Graeme Michael Campbell, PhD,† Jin Yamamura, MD,* Tobias Knopp, PhD,‡ Klaus Toedter, Dipl.-Chem,§ Roland Fischer, PhD,*|| Zhiyue Jerry Wang, PhD,¶ Alina Busch, MD,# Ann-Kathrin Ozga, PhD,** Shuo Zhang, PhD,† Thomas Lindner, PhD,* Florian Sevecke,‡ Mirco Grosser, MSc,‡ Gerhard Adam, MD,* and Patryk Szwarzgulski, MSc‡

Objectives: Fat quantification by dual-energy computed tomography (DECT) provides contrast-independent objective results, for example, on hepatic steatosis or muscle quality as parameters of prognostic relevance. To date, fat quantification has only been developed and used for source-based DECT techniques as fast kVp-switching CT or dual-source CT, which require a prospective selection of the dual-energy imaging mode.

It was the purpose of this study to develop a material decomposition algorithm for fat quantification in phantoms and validate it in vivo for patient liver and skeletal muscle using a dual-layer detector-based spectral CT (dlsCT), which automatically generates spectral information with every scan.

Materials and Methods: For this feasibility study, phantoms were created with 0%, 5%, 10%, 25%, and 40% fat and 0, 4.9, and 7.0 mg/mL iodine, respectively. Phantom scans were performed with the IQon spectral CT (Philips, the Netherlands) at 120 kV and 140 kV and 3 T magnetic resonance (MR) (Philips, the Netherlands) chemical-shift relaxometry (MRR) and MR spectroscopy (MRS). Based on maps of the photoelectric effect and Compton scattering, 3-material decomposition was done for fat, iodine, and phantom material in the image space.

After written consent, 10 patients (mean age, 55 ± 18 years; 6 men) in need of a CT staging were prospectively included. All patients received contrast-enhanced abdominal dlsCT scans at 120 kV and MR imaging scans for MRR.

As reference tissue for the liver and the skeletal muscle, retrospectively available non-contrast-enhanced spectral CT data sets were used. Agreement between dlsCT and MR was evaluated for the phantoms, 3 hepatic and 2 muscular regions of interest per patient by intraclass correlation coefficients (ICCs) and Bland-Altman analyses.

Results: The ICC was excellent in the phantoms for both 120 kV and 140 kV (dlsCT vs MRR 0.98 [95% confidence interval (CI), 0.94–0.99]; dlsCT vs MRS 0.96 [95% CI, 0.87–0.99]) and in the skeletal muscle (0.96 [95% CI, 0.89–0.98]). For log-transformed liver fat values, the ICC was moderate (0.75 [95% CI, 0.48–0.88]). Bland-Altman analysis yielded a mean difference of –0.7% (95% CI, –4.5 to 3.1) for the liver and of 0.5% (95% CI, –4.3 to 5.3) for the skeletal muscle. Interobserver and intraobserver agreement were excellent (>0.9).

Conclusions: Fat quantification was developed for dlsCT and agreement with MR techniques demonstrated for patient liver and muscle. Hepatic steatosis and myosteosis can be detected in dlsCT scans from clinical routine, which retrospectively provide spectral information independent of the imaging mode.

Key Words: dual-layer CT, spectral CT, material decomposition, detector-based dual-energy CT, phantom study, liver, hepatic steatosis, muscle quality, sarcopenia, myosteosis

(*Invest Radiol* 2022;57: 463–469)

Received for publication November 1, 2021; and accepted for publication, after revision, December 9, 2021.

From the *Department of Diagnostic and Interventional Radiology and Nuclear Medicine, University Medical Center Hamburg-Eppendorf; †Clinical Science, Philips GmbH Market DACH; ‡Institute for Biomedical Imaging, Technical University Hamburg, Section for Biomedical Imaging, University Medical Center Hamburg-Eppendorf; §Institute of Biochemistry and Molecular Cell Biology, University Medical Center Hamburg-Eppendorf, Hamburg, Germany; ||Hematology and Oncology Department, UCSF Benioff Children's Hospital Oakland, Oakland, CA; ¶Department of Radiology, Children's Health, The University of Texas Southwestern Medical Center, Dallas, TX; #Center for Oncology, 2nd Medical Clinic and Polyclinic, and **Institute of Medical Biometry and Epidemiology, University Medical Center Hamburg-Eppendorf, Hamburg, Germany.

Conflicts of interest and sources of funding: I.M. and P.S. received funding for interdisciplinary projects from the Hamburg Research Center for Medical Technology (04fmth2020). The coauthors G.M.C. and S.Z. are employees at Clinical Science of Philips. All other authors are independent and do not have any conflict of interest to declare. All data were generated, handled, and analyzed by the independent authors. No industry support was received for this project.

Data Availability Statement: The data sets generated during and/or analyzed during the current study are not publicly available, but are available from the corresponding author on reasonable request.

Correspondence to: Isabel Molwitz, MD, Department of Diagnostic and Interventional Radiology and Nuclear Medicine, University Medical Center Hamburg-Eppendorf, Martinistraße 52, 20246 Hamburg, Germany. E-mail: i.molwitz@uke.de.

Copyright © 2022 The Author(s). Published by Wolters Kluwer Health, Inc. This is an open-access article distributed under the terms of the Creative Commons Attribution-Non Commercial-No Derivatives License 4.0 (CCBY-NC-ND), where it is permissible to download and share the work provided it is properly cited. The work cannot be changed in any way or used commercially without permission from the journal.

ISSN: 0020-9996/22/5707–0463

DOI: 10.1097/RLI.0000000000000858

Since the introduction of new rapid kVp-switching computed tomography (CT) and dual-source CT scanners,¹ source-based dual-energy CT (DECT) techniques have increasingly become part of the clinical routine. In 2016, the first detector-based DECT scanner, the dual-layer spectral CT (dlsCT) was introduced. Its detector consists of 2 layers, an yttrium-based garnet scintillator and a bottom layer of gadolinium oxysulfide, which are sensitive to low and high energetic photons, respectively.² In contrast to source-based DECT techniques as fast kVp-switching CT or dual-source CT, it is advantageous that in dlsCT no dual-energy mode has to be chosen before imaging, which makes spectral information retrospectively available for every scan ≥120 kV.

With the measurement information from different energy levels as provided by DECT scanners, based on the photoelectric effect and the Compton scattering, which cause energy-specific attenuation coefficients for each material, material decomposition is feasible.³ Dual-energy CT material decomposition is applied for a broad range of clinical applications, among which iodine quantification, to provide perfusion information or to generate virtual noncontrast (VNC) images, is the most common and best evaluated, for both source- and detector-based DECT.⁴

Another application of DECT material decomposition concerns fat quantification, which has mainly been applied to detect hepatic steatosis as in the highly prevalent nonalcoholic fatty liver disease.⁵ Non-alcoholic fatty liver disease can progress to nonalcoholic steatohepatitis (NASH), which negatively influences survival in a variety of entities, for example, cancer,^{6,7} or after surgery.⁸ It is also a risk factor for hepatocellular carcinoma⁹ and the third most common cause of liver transplant.¹⁰ In contrast to invasive histology, subjective ultrasound, or

time-consuming magnetic resonance spectroscopy (MRS) with small measurement areas, liver fat quantification by DECT is objective, fast, and displays the whole organ. In comparison to fitting-based multiecho MR techniques, which require the resources for additional MR imaging (MRI) scans, it is advantageous that most chronically or seriously ill patients already receive CT scans regularly. Opposed to single-energy CT in DECT coexisting iron can be determined and does not lead to false-negative steatosis results.¹¹ Furthermore, DECT fat quantification results that are not influenced by contrast agent are relevant to characterize lesions, for example, of the adrenal gland,¹² and have recently been proposed as a more reliable radiological measure of myosteosis.¹³ Myosteosis is defined as fatty infiltration of the skeletal muscle and a parameter of muscle quality.¹⁴ This is of clinical relevance as measuring muscle quality is necessary to confirm the diagnosis of sarcopenia.¹⁵ Sarcopenia, which is a highly prevalent comorbidity in the elderly,¹⁶ is associated with high financial burdens for health care systems,^{17,18} lower quality of life,¹⁹ and mortality.²⁰ Furthermore, there is growing evidence that sarcopenia and especially myosteosis²¹ are associated with NASH and its severe clinical impact due to crosslinks in the pathology, for example, increasing insulin resistance with reduced muscle mass and quality.^{22,23} Techniques that objectively, rapidly, and without an additional patient burden allow to assess myosteosis and muscle quality are thus necessary.²⁴

However, although there are many studies on fat quantification in source-based DECT scanners as fast kVp-switching CT or dual-source CT, material decomposition for fat quantification in detector-based dlsCT has not been developed or evaluated so far.

Therefore, the objectives of this feasibility study were to develop material decomposition algorithms for detector-based dlsCT fat quantification in phantoms and to investigate their applicability for liver and muscle fat quantification in patients.

MATERIALS AND METHODS

Phantoms

Phantoms were created from distilled water, agar (Biovita Naturkost GmbH, Hameln, Germany), and 0%, 5%, 10%, 25%, and 40% volume percent of plant fat (Palmin; Peter Kölln GmbH, Elmshorn, Germany).

Plant fat was chosen due to its higher melting point, which resulted in more homogeneous phantoms than lard-based approaches. Each fat concentration series was generated with 0, 4.9, and 7.0 mg/mL iodine (Imeron 350; Bracco Imaging, Milan, Italy), which corresponds to concentrations in clinical abdominal CT scans if a patient blood volume between 4 and 5.7 L is assumed and 80 mL of contrast agent are injected. To increase the Compton and photoelectric attenuation of the water, agar mixture such that it was closer to that of liver tissue, 3 g of potassium (Kalinor; DESMA GmbH, Mainz-Kastel, Germany) was added to each phantom.

After the phantoms solidified, drilling cores were made via a 3D-printed (PreForm 2; Formlab, Somerville, MA) drill set and inserted into a multienergy CT phantom (Gammex; Sun Nuclear Corporation, Melbourne, Australia) (Fig. 1A).

Phantom Protocol and Measurements

Phantoms were scanned consecutively by dlsCT (Philips, Amsterdam, the Netherlands) and 3 T MRI (Philips, Amsterdam, the Netherlands).

Computed tomography collimation was 64×0.625 mm, pitch of 0.797, rotation time of 0.5 seconds, increment of 1 mm, and reconstructed slice thickness of 1 mm and 5 mm. Computed tomography scans were repeated at 120 kV, and 140 kV with a dose right index of 16, and the iDose reconstruction mode level 3 to correspond to clinical protocols in the department.

The MRI protocol (Philips, Amsterdam, the Netherlands) included a transverse 3D gradient echo sequence with 20 echo times (TEs; TE, 1.3/2.3 milliseconds; repetition time [TR], 24 milliseconds; flip angle [FA], 3 degrees) for MR chemical-shift relaxometry (MRR).

Furthermore, MRS PRESS sequences, which allowed correction for T2 effects, were acquired (TE, 30, 50, 70, and 90 milliseconds; TR, 5000 milliseconds; FA, 90 degrees; voxel size, $1.5 \times 1.5 \times 1.5$ cm³).

Patients

A total of $n = 10$ patients were prospectively included from the department of oncology between November 2020 and June 2021 after informed written consent. Defined inclusion criteria were the necessity of a CT scan for staging purposes and colorectal carcinoma under chemotherapy. Exclusion criteria were foreign bodies, which would cause

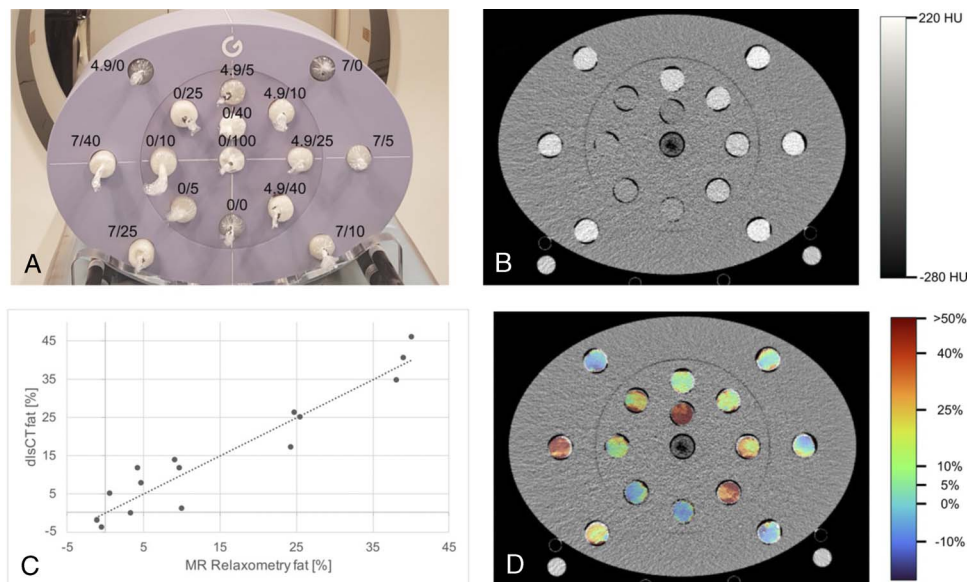


FIGURE 1. Measurement setup with iodine/fat concentrations (A), grayscale dual-layer spectral CT (dlsCT) image at 120 kV with a dose right index of 16 and reconstructed slice thickness of 1 mm (B), corresponding dlsCT fat concentrations versus results from MR relaxometry (C), and color-coded dlsCT fat concentration map.

CT artifacts or contraindications for MRI scans. The study protocol was approved by the local ethics committee (PV7006) and conducted in compliance with the Declaration of Helsinki.

Patient Protocol and Measurements

All participants received a clinically indicated dlsCT scan (Philips, Amsterdam, the Netherlands) and an additional 3 T MRI scan (Philips, Amsterdam, the Netherlands) of the liver and the skeletal muscle within 7 days (median, 0 days; range, 0–7 days).

Computed tomography scans were performed with 120 kV, a dose right index of 16 with boost for the liver (+3), and otherwise identical parameters as for the phantom scans. Image acquisition started 90 seconds after injection of 80 mL Imeron 350 (Bracco Imaging, Konstanz, Germany) with a flow rate of 2 mL/s.

The MRI protocol included a T2-weighted sagittal sequence (TE, 80 milliseconds; TR, 484 milliseconds; FA, 90 degrees) and transverse T1-weighted mDIXON sequences (TE, 1.3/2.3 milliseconds; TR, 3.7 milliseconds; FA, 10 degrees) of the liver and the muscle for anatomic orientation. Furthermore, transverse 3D gradient echo sequences with 20 TEs as used for the phantom scans were acquired of the liver and the muscle for MRR.

Magnetic resonance imaging muscle measurements were performed at the level of the third lumbar vertebra (L3), as single-energy CT body composition measurements of the skeletal muscle are acquired at that level.²⁵

Spectral Analysis

The dlsCT raw data were reconstructed and automatically converted to spectral base images (SBIs) on the dlsCT workstation. The data handling procedure is schematically shown in Figures 2A to C. Volumetric regions of interest (ROIs) were defined over the whole size of each phantom by a volumetric freeware (ITK-SNAP²⁶) and automatically transferred between the dlsCT scans at different kV.

Based on the respective attenuation coefficients of the Compton scattering and photoelectric effect, plots were generated, and 3-material decomposition was performed by solving a linear system of equations.^{27,28} Phantom scans were used to calibrate for the attenuation coefficients of fat, agar, and iodine at 120 kV and 140 kV, respectively. As the attenuation coefficients differ between hepatic and muscular tissue and cannot be derived from the phantom materials, additional reference values for the liver and muscle were necessary to apply the material decomposition to patient scans. Thus, reference values of the Compton scattering and photoelectric effect attenuation coefficients for the liver and the muscle were derived from retrospectively available non-contrast-enhanced dlsCT patient scans with existing informed written consent.

The relationship between the attenuation coefficients and the considered materials was then described using the matrix:

$$A = \begin{pmatrix} C_{fat} & C_{iodine} & C_{liver} \\ P_{fat} & P_{iodine} & P_{liver} \\ 1 & 1 & 1 \end{pmatrix} \in R^{3 \times 3}. \quad \text{Eq. 1}$$

Here, for each corresponding material C is the attenuation coefficient of the Compton scattering and P of the photoelectric effect. Material decomposition results are then obtained by calculating $A^{-1}b = x$, where $x = (x_{fat} \ x_{iodine} \ x_{liver})^T \in R^3$ is the result of the decomposition and $b = (C_{voxel} \ P_{voxel} \ 1)^T \in R^3$, with C_{voxel} being the attenuation coefficient of the Compton scattering and P_{voxel} of the photoelectric effect for each voxel. The first 2 equations of the linear system ensure that the superposition of fat, iodine, and liver values equals the measured value C_{voxel} respectively P_{voxel} and the third equation ensures that the tissue fraction in x add up to 1. Schematic display of material decomposition is provided in Figures 2C to D. Finally, the values within each of the phantoms and participants' ROIs were summarized by computing the respective mean (Table 1). To generate a visual impression, the liver and skeletal muscles were manually segmented in ITK-SNAP; color-coded fat maps were calculated and overlaid with the grayscale CT images (Figs. 3C, 4C).

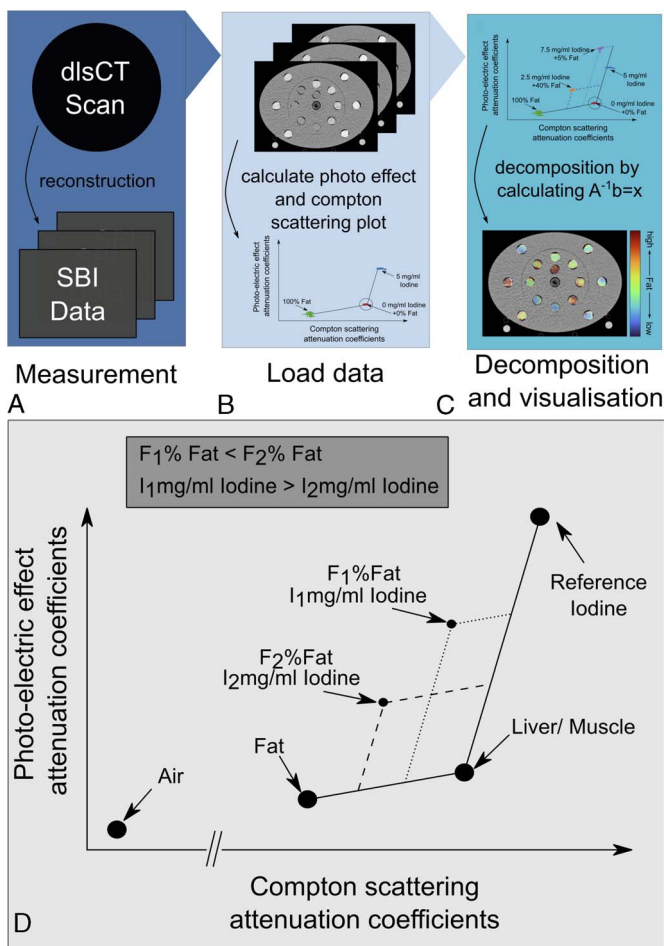


FIGURE 2. Dual-layer spectral CT (dlsCT) data handling (A–C) and schematic display of material decomposition (C, D). SBI, spectral base image.

Note that due to the fact that the calibrated attenuation coefficients of both the Compton scattering and photoelectric effect are set to one value and the measured data contain noise, negative results and results over 100% are possible.

Magnetic Resonance Imaging Analysis

For MRR, an in-house fitting algorithm²⁹ based on the spectral model of Hamilton et al³⁰ was applied to the first 7 echoes of the magnitude images. To determine the muscular fat amount, the main methylene peak was fitted between the lipid peaks for intramyocellular lipid (1.3 ppm, 434 Hz) and extramyocellular lipid (1.5 ppm, 409 Hz).

In the phantoms, 2D ROIs were defined over the whole phantom size. In the patients, 3 ROIs were defined distant to large vessels within the periphery of the caudal right liver lobe, which is less prone to respiratory movements³¹ (Fig. 3B). Two ROIs were defined within the inner borders of the posterior paraspinal muscle at both sides of the spine (Fig. 4B). All ROIs were independently drawn by a radiologist in-training with 3 years of experience (twice with >1 week delay for intraobserver analysis) and a radiologist with 16 years of experience.

Statistics

Data were characterized by the mean values with standard deviation or median (for skewed distributions) and range. For correlation of phantom fat concentrations in dlsCT, MRR, and MRS, Spearman correlation coefficient was used. Absolute agreement between the techniques in phantoms and participants was evaluated by the 1-way random intraclass correlation coefficient (ICC). As distribution of the liver ROI measurement

TABLE 1. dlsCT and MRR Results With SD for the Mean of 3 ROIs in the Liver and the ROIs in the Skeletal Muscle at Both Sides of the Spine

| No. | Sex | Age | BMI | Liver | | Muscle Right Side | | Muscle Left Side | |
|-----|-----|-----|------|---------------|-------------|-------------------|-------------|------------------|-------------|
| | | | | dlsCT (SD), % | MRR (SD), % | dlsCT (SD), % | MRR (SD), % | dlsCT (SD), % | MRR (SD), % |
| 1 | F | 35 | 18.2 | 1.3 (1.1) | 0.9 (0.7) | 2.8 (0.7) | 2.0 (0.5) | 1.2 (1.5) | 2.2 (0.3) |
| 2 | M | 81 | 26.5 | 18.1 (1.7) | 18.2 (0.9) | 12.1 (9.8) | 11.5 (1.5) | 11.2 (8.1) | 12.2 (2.4) |
| 3 | M | 50 | 25.0 | 5.5 (1.4) | 9.7 (2.4) | 2.5 (2.0) | 1.3 (0.1) | -0.1 (.3) | 1.7 (0.1) |
| 4 | M | 38 | 30.4 | 3.0 (1.5) | 2.0 (1.9) | 1.9 (1.4) | 1.5 (0.4) | 1.8 (1.7) | 3.3 (0.4) |
| 5 | M | 73 | 21.4 | 1.0 (1.3) | 1.9 (0.5) | 12.6 (4.3) | 12.1 (1.5) | 18.7 (5.5) | 14.0 (1.1) |
| 6 | F | 52 | 29.6 | 4.3 (1.2) | 7.4 (0.7) | 8.1 (5.0) | 4.9 (0.4) | 8.4 (1.6) | 5.5 (0.5) |
| 7 | F | 32 | 18.1 | 2.1 (1.0) | 0.8 (0.8) | -0.5 (0.7) | 1.8 (0.4) | 0.6 (1.1) | 2.6 (0.3) |
| 8 | M | 68 | 23.7 | 1.2 (1.2) | 1.4 (0.7) | 9.4 (2.7) | 8.4 (0.6) | 10.5 (2.5) | 14.5 (1.2) |
| 9 | F | 52 | 33.7 | 5.7 (1.4) | 6.2 (1.0) | 6.2 (0.9) | 5.3 (0.4) | 7.2 (1.8) | 5.3 (0.3) |
| 10 | M | 73 | 26.9 | -1.2 (1.6) | 1.5 (0.6) | 10.2 (3.8) | 12.8 (2.8) | 11.0 (2.5) | 11.8 (2.5) |

dlsCT, dual-layer detector-based spectral CT; MRR, chemical-shift relaxometry; ROI, region of interest; BMI, body mass index; F, female; M, male.

results was right skewed in dlsCT and MRR, they were log-transformed to generate approximately normally distributed data. Intraobserver and interobserver agreement for dlsCT were evaluated by the 2-way mixed ICC testing for absolute agreement. The mean difference between dlsCT and MRR for the liver and the skeletal muscle was given by Bland-Altman analyses. All analyses were conducted in IBM SPSS Statistics Version 26. There were no missing data to be considered. Because of the explorative study design, *P* values are considered descriptive.

RESULTS

Phantom Results

As indicated by the color-coded maps of phantom fat concentrations (Fig. 1D), fat distribution within the phantoms was mostly homogeneous. With calibration for the respective attenuation coefficients of the Compton scattering and photoelectric effect at 120 kV and 140 kV, the mean difference between fat quantification results at both voltages was $0.002\% \pm 1.2\%$.

Correlation between dlsCT and MR was excellent with $r = 0.92$ for MRR (Fig. 1C) and $r = 0.93$ for MRS, at both 120 kV and 140 kV. All *P* values were <0.01 . The ICC between dlsCT, for both 120 kV and 140 kV, and MRR was 0.98 (95% confidence interval [CI], 0.94–0.99); between dlsCT and MRS, it was 0.96 (95% CI, 0.87–0.99).

Study Collective and Patient Results

The patient collective consisted of $n = 10$ participants (6 male, 4 female) (Table 1). No patient dropped out during the study. The mean age was 55 ± 18 years; the mean body mass index was 25.3 ± 5.1 kg/m².

The median dlsCT fat value of the averaged 3 defined liver ROIs was 2.6%, with a minimum of -1.2% and a maximum of 18.1% (Table 1). Within the 2 ROIs of the skeletal muscle, dlsCT mean fat values were higher with 6.8%, but with a comparable range of -0.5% to 18.7% (Table 1). Muscle values differed between the left and right sides of the participants with a mean of $6.5\% \pm 4.6\%$ on the right side and $7.0\% \pm 6.1\%$ on the left side of the spine in dlsCT. Women showed higher median hepatic ($3.2\% \pm 2.0\%$) and smaller mean muscular ($4.3\% \pm 3.6\%$) fat concentrations than men ($2.1\% \pm 7.0\%$; $9.1\% \pm 5.7\%$). Visual impression of hepatic and muscular fat distribution for 2 exemplary patients is provided in Figure 3 and Figure 4.

The dlsCT results of all voxels within the defined liver and muscle ROIs were homogeneous, except for some outliers with an interquartile range between 0.8% and 6.3% (Fig. 5A). Absolute agreement between dlsCT and MRR was found to be moderate for the log-transformed liver ROIs ($r = 0.75$ [95% CI, 0.48–0.88]) and excellent for the originally normally distributed muscle ROI data ($r = 0.96$ [95% CI, 0.89–0.98]). Bland-Altman analysis yielded a mean difference of -0.7% (95% CI, -4.5 to 3.1) for the liver and of 0.5% (95% CI, -4.3 to 5.3) for the skeletal muscle (Figs. 5B, C).

Interobserver and intraobserver agreement for both the liver (0.90 [0.8–0.95]; 0.93 [0.85–0.97]) and the muscle (0.99 [0.98–1.0]; 0.97 [0.93–1.0]) were excellent.

DISCUSSION

To date, fat quantification has only been used for source-based DECT. Therefore, in this study, material decomposition for fat quantification was developed for dlsCT by phantom measurements and applied to patient liver and skeletal muscle.

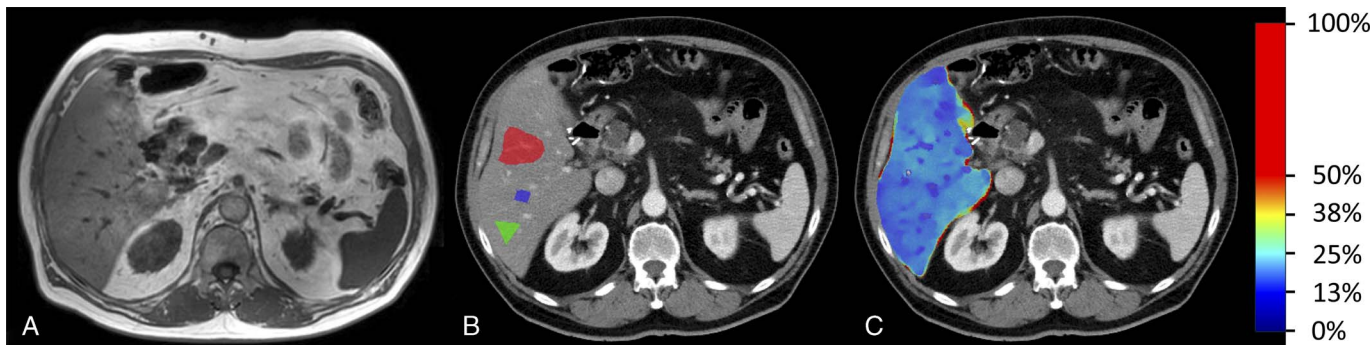


FIGURE 3. MR mDIXON image (A), grayscale dual-layer spectral CT (dlsCT) images (reconstructed slice thickness 5 mm) with regions of interest (B), and with color-coded overlay of material decomposition fat concentration results for the liver.

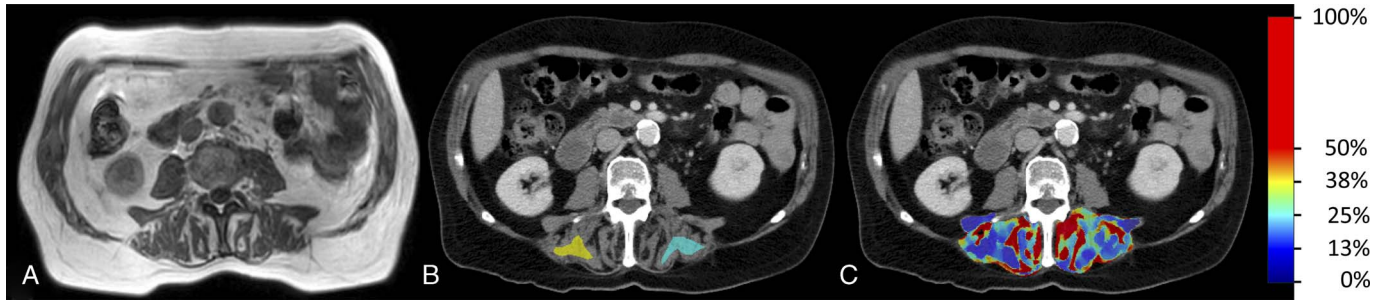


FIGURE 4. MR mDIXON image (A), grayscale dual-layer spectral CT (dlsCT) images (reconstructed slice thickness 5 mm) with regions of interest (B), and with color-coded overlay of material decomposition fat concentration results for the posterior paraspinal muscle.

DlsCT fat quantification results were in excellent agreement with MRS and MRR results in the phantoms ($r > 0.9$). When applied in vivo to patient liver and skeletal muscle, dlsCT agreed well with MRR and mean differences were small.

In contrast to source-based DECT, it is a major technical benefit of dlsCT that spectral information is automatically given for all scans ≥ 120 kV. Thus, no prospective selection of a dual-energy imaging mode is necessary and retrospective fat quantification is feasible, for example, to validate a morphologically suspected hepatic steatosis or myosteatorsis.

With regards to the technical approach, material decomposition in this study, as in previous works for dual-source CT,³ was done by using linear equations based on the Compton scattering and photoelectric effect, which were calibrated for the 3 used materials (fat, iodine, liver/muscle). Other approaches described for source-based DECT techniques include multimaterial decomposition,²² which would be rel-

evant if fat quantification and color-coded fat maps were to be generated for different organs simultaneously, as the respective Compton and photoelectric attenuations of, for example, muscle, are located on the vector between fat and liver.

When calibrated to the scan voltage, fat quantification results at different kV were found to agree well. Data sets of 120 kV and 140 kV can thus both be used for retrospective analyses. Given prior calibration for the Compton and photoelectric attenuation, the findings of this study should also be applicable for other dlsCT scanner types.

Furthermore, as in all DECT techniques, it is advantageous that fat material decomposition results are not influenced by the use and phase of contrast agent,³¹ which is opposed to HU values used for steatorsis detection and measurement of muscle density in single-energy CT. Moreover, even if care should be taken when comparing VNC values between different scanner types such as source-based DECT or dlsCT,³² it should also be feasible to analyze HU values on dlsCT

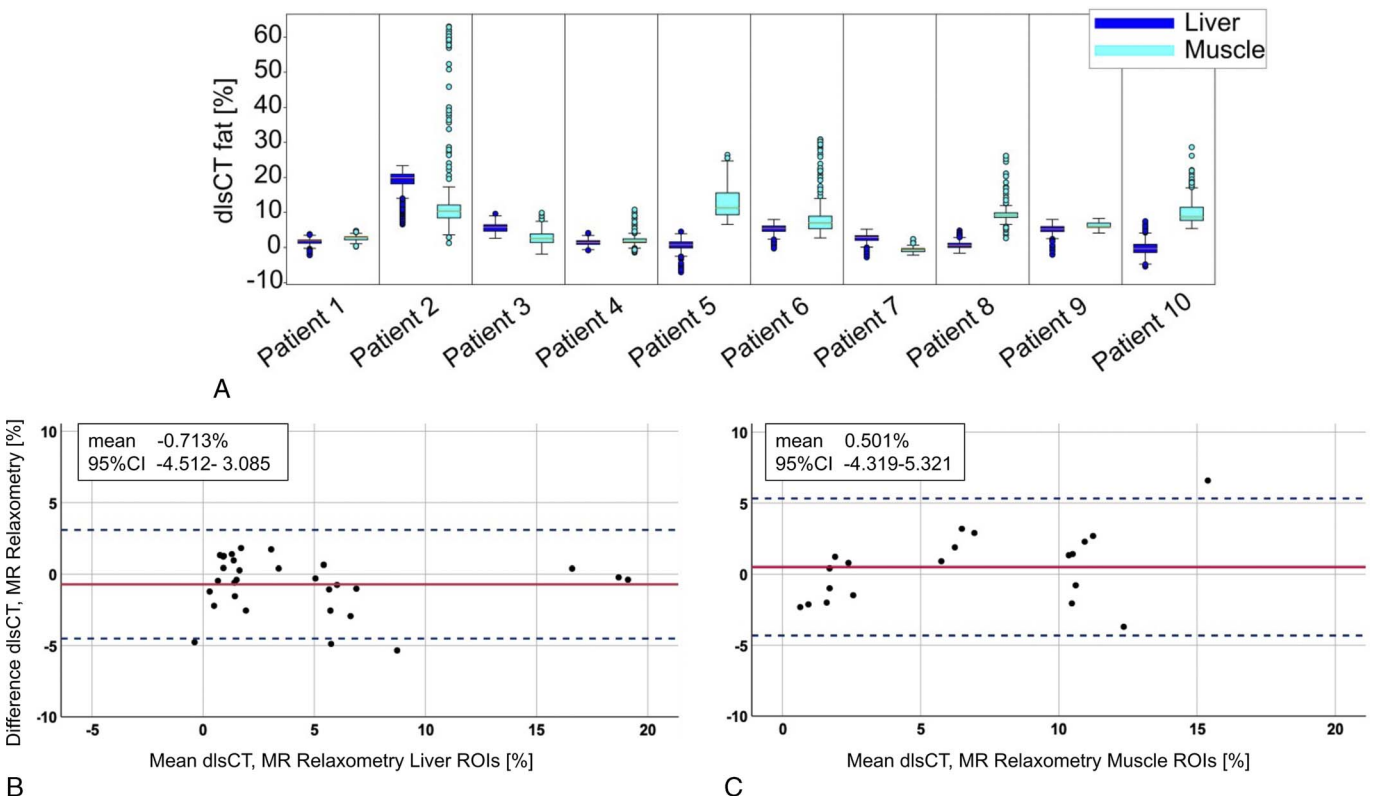


FIGURE 5. Distribution of dual-layer spectral CT (dlsCT) results for each voxel within all defined regions of interest (ROI) in the liver and the skeletal muscle (A) and Bland-Altman analyses for fat quantification results in dlsCT and MR relaxometry for the liver (B) and the skeletal muscle (C).

VNC maps, as these have been shown to differ less than 15 HU compared with real non-contrast-enhanced dlsCT HU values.³³

As this is the first study on fat quantification in dlsCT, results can only be compared with source-based DECT studies.

For the liver, the mean difference including upper and lower 95% limits of agreement of dlsCT and MRR (−0.7% [95% CI, −4.5 to 3.1]) was better than published by Hur et al³⁴ for fast kVp-switching CT and MR proton density in rabbit liver (1.56% [95% CI, −8.7 to 11.8]) and slightly better than the results of Gassenmaier et al³⁵ for dual-source DECT and a multiecho DIXON MRI sequence in patient liver (−1.7% [95% CI, −7.3 to 3.9]). Although the ICC for the liver was lower than for the skeletal muscle, as data were right skewed, which required log-transformation, the agreement ($r = 0.75$ [95% CI, 0.48–0.88]) was comparable to that of Artz et al³⁶ for fast kVp-switching CT and mice liver ($r^2 \leq 0.67$), and better than that of Kramer et al³⁷ for fast kVp-switching CT and MRS in patients ($r^2 = 0.423$).

Overall, studies on DECT fat quantification in the skeletal muscle are rare and only exist for dual-source CT. Besides one study that described correlation of dual-source CT results to the morphological appearance of muscular fatty infiltration in the rotator cuff,³⁸ there are 2 studies that verified dual-source CT fat quantification by MRI, both with a focus on the paraspinal muscle. Compared with the first study from 2020,¹³ the agreement for dlsCT and MRR in this study was slightly better ($r = 0.83^{13}$ vs $r = 0.96$). Concerning the mean difference and 95% limits of agreement, the results for the skeletal muscle by dlsCT in this study (0.5% [95% CI, −4.3 to 5.3]) are comparable (and even identical) to the ranges published by both studies on dual-source CT (0.15% [95% CI, −6.66 to 6.35]¹³; 0.5% [95% CI −4.3 to 5.3]³⁵).

For both detection of hepatic steatosis and myosteatosis, the independence of dlsCT fat quantification from the iodine content in the issue is beneficial, as most abdominal routine CT protocols, for example, for cancer staging, search of infection, or in trauma patients, require contrast agent. For the skeletal muscle, dlsCT fat quantification is of special relevance, because bioelectrical impedance analysis as the commonly used technique in clinical routine is influenced by the patient's hydration status,³⁹ and radiological methods are considered the criterion standard to assess muscle mass and quality to confirm a suspected sarcopenia.^{15,40} However, the muscle radiodensity in HU, which is used to indirectly assess myosteatosis and thus muscle quality¹⁴ in single-energy CT, is influenced by contrast agent. In addition, it is problematic that, as 2 recent reviews^{25,41} demonstrate, most studies (66.7% of 117²⁵; 94% of 388⁴¹) on the muscle radiodensity do not provide information on whether contrast agent was used and in which scan phase contrast-enhanced images were acquired. This hinders comparability and highlights the benefit of material decomposition and quantified muscle fat values, which are not influenced by contrast agent. Furthermore, because the single-energy CT skeletal muscle index, as a parameter of muscle quantity, does not consider volume overload or intramyocellular fat deposits, and muscle characterization using MRI is resource intensive, new standardized techniques to determine muscle quality objectively are expected to gain importance.^{15,24} This could prospectively include dlsCT fat quantification.

A limitation of this study was the low liver fat values in the majority of patients, which resulted in right-skewed data for the liver ROIs and the necessity of log-transformation before calculation of the ICC. However, when comparing the results from the Bland-Altman analyses for the liver and the muscle, agreement of dlsCT and MRR is comparably high for both organs.

For some ROIs, the average dlsCT voxel results were negative because the measured data, reconstructed images, and thus the calculated fat maps contain noise, which despite noise reduction cannot be completely eliminated. However, this is a common issue for values close to zero in commercially available software for dual-source DECT, as well.

As this was a study on experimental development of dlsCT fat quantification with application in first patients, participant numbers

were low. In future studies, the accuracy of dlsCT fat quantification for the liver and the muscle, as well for other organs, for example, for incidentaloma or tumor characterization, should be evaluated in larger collectives. Furthermore, it will be necessary to investigate dlsCT accuracy in coexisting hepatic fat and iron overload, as done for dual-source DECT.¹¹ To improve applicability in large cohorts and for clinical routine, the implementation of an automated segmentation as recently published for the skeletal muscle by Nowak et al⁴² should be evaluated. It would also be of interest to investigate the relation of dlsCT fat values and single-energy CT values, which could be assessed from dlsCT VNC maps to avoid the additional radiation exposure of a second scan, and their respective impact on clinical parameters.

In conclusion, in this study, detector-based dlsCT fat quantification was developed in phantoms and successfully used to determine hepatic and muscular fat concentrations in patients. With this method hepatic steatosis and reduced muscle quality, as parameters of prognostic relevance, can be detected in clinical routine dlsCT scans. This is beneficial, as in contrast to source-based DECT techniques, detector-based dlsCT does not require a prospective selection of a dual-energy imaging mode and thus retrospectively provides spectral information for every scan ≥ 120 kV.

REFERENCES

- Flohr TG, McCollough CH, Bruder H, et al. First performance evaluation of a dual-source CT (DSCT) system. *Eur Radiol.* 2006;16:256–268.
- Rassouli N, Etesami M, Dhanantwari A, et al. Detector-based spectral CT with a novel dual-layer technology: principles and applications. *Insights Imaging.* 2017;8:589–598.
- Johnson TR, Krauss B, Sedlmair M, et al. Material differentiation by dual energy CT: initial experience. *Eur Radiol.* 2007;17:1510–1517.
- McCollough CH, Leng S, Yu L, et al. Dual- and multi-energy CT: principles, technical approaches, and clinical applications. *Radiology.* 2015;276:637–653.
- Chalasan N, Younossi Z, Lavine JE, et al. The diagnosis and management of non-alcoholic fatty liver disease: practice guideline by the American Association for the Study of Liver Diseases, American College of Gastroenterology, and the American Gastroenterological Association. *Hepatology.* 2012;55:2005–2023.
- Wu K, Zhai MZ, Weltzien EK, et al. Non-alcoholic fatty liver disease and colorectal cancer survival. *Cancer Causes Control.* 2019;30:165–168.
- Chen H, Dai S, Fang Y, et al. Hepatic steatosis predicts higher incidence of recurrence in colorectal cancer liver metastasis patients. *Front Oncol.* 2021;11:631943.
- Veteläinen R, van Vliet A, Gouma DJ, et al. Steatosis as a risk factor in liver surgery. *Ann Surg.* 2007;245:20–30.
- Anstee QM, Reeves HL, Kotsiliti E, et al. From NASH to HCC: current concepts and future challenges. *Nat Rev Gastroenterol Hepatol.* 2019;16:411–428.
- Zezos P, Renner EL. Liver transplantation and non-alcoholic fatty liver disease. *World J Gastroenterol.* 2014;20:15532–15538.
- Ma J, Song ZQ, Yan FH. Separation of hepatic iron and fat by dual-source dual-energy computed tomography based on material decomposition: an animal study. *PLoS One.* 2014;9:e110964.
- Ju Y, Liu A, Dong Y, et al. The value of nonenhanced single-source dual-energy CT for differentiating metastases from adenoma in adrenal glands. *Acad Radiol.* 2015;22:834–839.
- Molwitz I, Leiderer M, McDonough R, et al. Skeletal muscle fat quantification by dual-energy computed tomography in comparison with 3T MR imaging. *Eur Radiol.* 2021;31:7529–7539.
- Rahemi H, Nigam N, Wakeling JM. The effect of intramuscular fat on skeletal muscle mechanics: implications for the elderly and obese. *J R Soc Interface.* 2015;12:20150365.
- Cruz-Jentoft AJ, Bahat G, Bauer J, et al. Sarcopenia: revised European consensus on definition and diagnosis. *Age Ageing.* 2019;48:16–31.
- Shafiee G, Keshkar A, Soltani A, et al. Prevalence of sarcopenia in the world: a systematic review and meta-analysis of general population studies. *J Diabetes Metab Disord.* 2017;16:21.
- Antunes AC, Araujo DA, Verissimo MT, et al. Sarcopenia and hospitalisation costs in older adults: a cross-sectional study. *Nutr Diet.* 2017;74:46–50.
- Mijnarends DM, Luijing YC, Halfens RJG, et al. Muscle, health and costs: a glance at their relationship. *J Nutr Health Aging.* 2018;22:766–773.
- Beaudart C, Biver E, Reginster JY, et al. Validation of the SarQoL®, a specific health-related quality of life questionnaire for sarcopenia. *J Cachexia Sarcopenia Muscle.* 2017;8:238–244.

20. De Buyser SL, Petrovic M, Taes YE, et al. Validation of the FNIH sarcopenia criteria and SOF frailty index as predictors of long-term mortality in ambulatory older men. *Age Ageing*. 2016;45:602–608.
21. Nachit M, De Rudder M, Thissen JP, et al. Myosteatosis rather than sarcopenia associates with non-alcoholic steatohepatitis in non-alcoholic fatty liver disease pre-clinical models. *J Cachexia Sarcopenia Muscle*. 2021;12:144–158.
22. Cleasby ME, Jamieson PM, Atherton PJ. Insulin resistance and sarcopenia: mechanistic links between common co-morbidities. *J Endocrinol*. 2016;229:R67–R81.
23. Kim JA, Choi KM. Sarcopenia and fatty liver disease. *Hepatol Int*. 2019;13:674–687.
24. Correa-de-Araujo R, Harris-Love MO, Miljkovic I, et al. The need for standardized assessment of muscle quality in skeletal muscle function deficit and other aging-related muscle dysfunctions: a symposium report. *Front Physiol*. 2017;8:87.
25. Poltronieri TS, de Paula NS, Chaves GV. Assessing skeletal muscle radiodensity by computed tomography: an integrative review of the applied methodologies. *Clin Physiol Funct Imaging*. 2020;40:207–223.
26. Yushkevich PA, Piven J, Hazlett HC, et al. User-guided 3D active contour segmentation of anatomical structures: significantly improved efficiency and reliability. *Neuroimage*. 2006;31:1116–1128.
27. Alvarez RE, Macovski A. Energy-selective reconstructions in x-ray computerized tomography. *Phys Med Biol*. 1976;21:733–744.
28. Mendonca PR, Lamb P, Sahani DV. A flexible method for multi-material decomposition of dual-energy CT images. *IEEE Trans Med Imaging*. 2014;33:99–116.
29. Pfeifer CD, Schoennagel BP, Grosse R, et al. Pancreatic iron and fat assessment by MRI-R2* in patients with iron overload diseases. *J Magn Reson Imaging*. 2015;42:196–203.
30. Hamilton G, Yokoo T, Bydder M, et al. In vivo characterization of the liver fat 1H MR spectrum. *NMR Biomed*. 2011;24:784–790.
31. Tsai YL, Wu CJ, Shaw S, et al. Quantitative analysis of respiration-induced motion of each liver segment with helical computed tomography and 4-dimensional computed tomography. *Radiat Oncol*. 2018;13:59.
32. Lennartz S, Pisuchpen N, Parakh A, et al. Virtual unenhanced images: qualitative and quantitative comparison between different dual-energy CT scanners in a patient and phantom study. *Invest Radiol*. 2022;57:52–61.
33. Adam SZ, Rabinowich A, Kessner R, et al. Spectral CT of the abdomen: where are we now? *Insights Imaging*. 2021;12:138.
34. Hur BY, Lee JM, Hyunsik W, et al. Quantification of the fat fraction in the liver using dual-energy computed tomography and multimaterial decomposition. *J Comput Assist Tomogr*. 2014;38:845–852.
35. Gassenmaier S, Kahm K, Walter SS, et al. Quantification of liver and muscular fat using contrast-enhanced dual source dual energy computed tomography compared to an established multi-echo Dixon MRI sequence. *Eur J Radiol*. 2021;142:109845.
36. Artz NS, Hines CD, Brunner ST, et al. Quantification of hepatic steatosis with dual-energy computed tomography: comparison with tissue reference standards and quantitative magnetic resonance imaging in the Ob/Ob mouse. *Invest Radiol*. 2012;47:603–610.
37. Kramer H, Pickhardt PJ, Kliewer MA, et al. Accuracy of liver fat quantification with advanced CT, MRI, and ultrasound techniques: prospective comparison with MR spectroscopy. *AJR Am J Roentgenol*. 2017;208:92–100.
38. Baillargeon AM, Baffour FI, Yu L, et al. Fat quantification of the rotator cuff musculature using dual-energy CT-A pilot study. *Eur J Radiol*. 2020;130:109145.
39. Heymsfield SB, Gonzalez MC, Lu J, et al. Skeletal muscle mass and quality: evolution of modern measurement concepts in the context of sarcopenia. *Proc Nutr Soc*. 2015;74:355–366.
40. Beaudart C, McCloskey E, Bruyere O, et al. Sarcopenia in daily practice: assessment and management. *BMC Geriatr*. 2016;16:170.
41. Amini B, Boyle SP, Boutin RD, et al. Approaches to assessment of muscle mass and myosteatosis on computed tomography: a systematic review. *J Gerontol A Biol Sci Med Sci*. 2019;74:1671–1678.
42. Nowak S, Faron A, Luetkens JA, et al. Fully automated segmentation of connective tissue compartments for CT-based body composition analysis: a deep learning approach. *Invest Radiol*. 2020;55:357–366.